Arctic Sea Ice Thickness Estimation From Passive Microwave Satellite Observations Between 1.4 and 36 GHz

Clément Soriot, Catherine Prigent, Carlos Jimenez, Frédéric Frappart

![AGU ADVANCING EARTH AND SPACE SCIENCE]

Earth and Space Science

Key Points:

- High correlation is evidenced over the Arctic between passive microwave (PMW) satellite signatures and sea ice thickness (SIT) derived from lidar and radar altimeters
- A Neural Network inversion is developed to mimic lidar-derived SIT, with PMW observations
- SIT estimates from passive microwaves show good performances when compared to other satellite or modeled SIT, and to campaign measurements

Correspondence to:

C. Soriot,
clement.soriot@observatoiredeparis.psl.eu

Arctic Sea Ice Thickness Estimation From Passive Microwave Satellite Observations Between 1.4 and 36 GHz

Clément Soriot[1] , Catherine Prigent[1,2], Carlos Jimenez[1,2], and Frédéric Frappart[3]

[1]LERMA, Paris Observatory, CNRS, PSL, Paris, France, [2]Estellus, Paris, France, [3]ISPA, INRAE/Bordeaux Sciences Agro, Bordeaux, France

Abstract Arctic sea ice thickness (SIT) has been mostly retrieved from lidar and radar altimeters since the 2000s. However, the repeatability of altimeters and their spatial coverage limit SIT estimates spatially and temporally. On the other hand, the passive microwave (PMW) radiometers have daily basin-scale coverage of the Arctic. In this study, we propose a SIT retrieval from PMW observations, derived from a statistical inversion technique. It is based on the evidence of high correlations between PMW observations and existing altimetric satellite-derived SIT, especially at 36 GHz. Lidar ICESat-2 SIT products are used to train a neural network with multiple combinations of brightness temperatures between 1.4 and 36 GHz as inputs over the 2018–2019 time period. The PMW retrieved SIT can mimic the lidar SIT product over the full winter over the Arctic, with a correlation of 0.85, and a root mean square difference (RMSD) of 0.54 cm. Results are also compared with the SIT product CS2SMOS (CryoSat-2 and Soil Moisture Ocean Salinity merged product), with SIT from a coupled ice/ocean reanalysis model and with the Operation IceBridge QuickLook airborne SIT measurements. The PMW SIT retrieval with all frequencies from 1.4 to 36 GHz shows a correlation of 0.72 and a RMSD of 57 cm when compared to OIB-QL measurements, for large SIT (mostly above 3 m), under multi-year ice environments. The PMW SIT retrieval using only 18 and 36 GHz has similar performances and could allow the calculation of long time series, these microwave frequencies being available from satellites since the 1980s.

Plain Language Summary Arctic sea ice thickness (SIT) has been estimated from satellite radar and lidar altimeters since the 2000s. However, the altimeter spatial coverage and their repeatability limit the SIT estimates, spatially and temporally. On the other hand, satellite passive microwave (PMW) radiometers have daily basin-scale coverage of the Arctic. In this study, we estimate SIT from PMW observations, with a statistical inversion technique. It is based on the evidence of a high absolute correlation between existing altimetric satellite-derived SIT, and PMW observations, especially at 36 GHz. Lidar SIT products are used to train a neural network with multiple combinations of PMW observations between 1.4 and 36 GHz as inputs, over the 2018–2019 time period. Results are compared with other satellite and model derived SIT, as well as with airborne campaign measurements. The new PMW SIT retrieval with all frequencies from 1.4 to 36 GHz shows good performance, even for large SIT, under multi-year ice environments. The SIT retrieval using only 18 and 36 GHz also has satisfactory performances, allowing the development of long time series, these two microwave frequencies being available from satellites since the 1980s.

1. Introduction

Over the last decades, the Arctic region has experienced climate changes at magnitudes and rates higher than most regions in the world (IPCC report, 2019) leading to a large decrease in sea ice extent (SIE) and thickness (SIT) (Pörtner et al., 2019). Sea ice regulates the energy and mass exchange between the atmosphere and the underlying ocean in the polar regions, and the observed sea ice loss over the last ~40 years contributed to the warming amplification in the boreal region (e.g., Dai et al., 2019; Serreze & Barry, 2011).

The SIE has been extensively monitored from passive microwave (PMW) satellite observations since the late 70s (e.g., Comiso, 1986), and its decline has been evidenced (e.g., Kwok, 2018; Stroeve et al., 2012). Large-scale satellite estimation of the SIT, the other necessary parameter to estimate the sea ice volume, is more recent, with the advent of the laser altimeter missions (Ice, Cloud and Land Elevation Satellite (ICESat and ICESat-2) (Abdalati et al., 2010; Schutz et al., 2005)), and radar altimeter missions (e.g., ERS 1 and 2 (S. Laxon et al., 2003), ENVISAT (Connor et al., 2009) or CryoSat-2 (CS2) (S. W. Laxon et al., 2013; Wingham et al., 1986), see Abdalla et al. (2021)

Writing – review & editing: Clément Soriot, Frédéric Frappart

for a review). Because of their nadir geometry, the repeatability of altimeters and their spatial coverage limit SIT estimates spatially and temporally. Both altimetry techniques (laser and radar) estimate a freeboard, that is, the thickness of the layer protruding above the water level: for the laser altimeters, this layer includes the snow cover and for the low frequency radar, the signal is expected to penetrate the snow layer and reach the sea ice surface. The freeboard estimate is the difference between a measurement above sea ice and another one over open ocean or a lead. The estimation of the total SIT, including the submerged draft sea ice part, always assumes hydrostatic equilibrium, and an estimation of the snow loading over the sea ice. As a consequence, assumptions have to be made, first on the snow depth and density, often using climatologies (Warren et al., 1999), but also satellite estimates or modeling, and second on the ice and water densities. Long time series of publicly available SIT products include the ICESat-2 monthly winter product from Petty et al. (2020) or the CS2 winter product from Tilling et al. (2018). The sensitivity of the radar altimeter is expected to decrease for low SIT. On the contrary, passive microwaves at L-Band (1.4 GHz), from the Soil Moisture Ocean Salinity (SMOS, Font et al. (2010)) or the Soil Moisture Active Passive (SMAP, Entekhabi et al. (2010)) missions, have shown sensitivity to thin SIT. The merging of CS2 and SMOS SIT products has led to an improved product (CS2SMOS) covering the full range of SIT, over winter (Ricker et al., 2014).

Satellite-based SIT estimates have been evaluated and compared. Wang et al. (2016) include ICESat-2, CS2, and SMOS products in their comparison against aircraft and model estimates. Sallila et al. (2019) essentially concentrate on the differences between radar altimeter products derived from CS2. In addition to the intrinsic limitations of the different satellite sensors, estimations of SIT are based on several and different assumptions on the snow load and the geophysical parameters of the sea ice, which leads to differences between SIT products (Petty et al., 2020; Wang et al., 2016), even when using the same instrument (Sallila et al., 2019).

Satellite PMW observations have been extensively exploited to estimate Sea Ice Concentration (SIC and the related SIE), sea ice type, as well as snow depth over sea ice, mainly from 18 to 36 GHz measurements from imagers such as the Advanced Microwave Scanning Radiometers or the Special Sensor Microwave/Imagers (SSM/I) (Comiso, 1995; Comiso et al., 2003; Lavergne et al., 2019; Markus & Cavalieri, 2009; Walker et al., 2006). Thin SIT is also now routinely estimated from passive microwaves at 1.4 GHz (Kaleschke et al., 2016). Efforts are also conducted to estimate thin SIT with higher frequencies (18 and 36 GHz) (e.g., Yoshizawa et al., 2018 or Kashiwase et al., 2021). However, evaluation of the potential of the PMW observations to estimate the SIT for the full thickness range has not triggered yet much efforts, as PMW observations are not expected to penetrate the ice for more than 50 cm, and to be directly sensitive to the thicker sea ice, especially at high frequency (Heygster et al., 2014). Nevertheless, we observed unexpected systematic high correlation at basin-scale between PMW observations and existing SIT, during the full winter (see sections below). Recently, Lee et al. (2021) proposed an estimation of the SIT in the Arctic, from the Advanced Microwave Scanning Radiometer 2 (AMSR2, Imaoka et al. (2012)) frequencies between 6 and 36 GHz, based on the assumed proportionality between the scattering optical thickness at these frequencies within the freeboard and the physical thickness of the freeboard, and a realistic snow depth on sea ice. The relationship between the optical thickness and the ice freeboard is derived from a linear fit with ice freeboard from CS2. Chi and Kim (2021) suggested a complex NN method to mimic the CryoSat-2 SIT retrievals, with AMSR2 observations.

Here, we also propose to directly exploit the statistical relationships observed between the PMW observations and the existing large-scale SIT estimates, to derive SIT using a machine-learning approach. The motivation is twofold: first to develop a method to produce a robust long-time record of sub-monthly SIT with almost full coverage of the Arctic basin, second to prepare for the exploitation of the Copernicus Imaging Microwave Radiometer (CIMR) mission. Copernicus Imaging Microwave Radiometer (Donlon, 2020; Kilic et al., 2018) is a Copernicus High Priority Expansion Mission designed to monitor the poles. It will observe from 1.4 to 36 GHz, with a large ~8 m antenna to reach 5 km spatial resolution at 18 and 36 GHz. The Copernicus Polar Ice and Snow Topography Altimeter, CRISTAL, another Copernicus High Priority Expansion Mission, will also measure the SIT, overlying snow depth and ice sheet elevations, owing to a dual frequency altimeter operating at Ku (13.5 GHz) and Ka (36.5 GHz) bands, and synergies between these two CIMR and CRISTAL are encouraged.

A database with observations at CIMR frequencies is built, merging the SMAP observations at 1.4 GHz and the AMSR2 ones at 6, 10, 18, and 36 GHz, to characterize sea ice and snow (Soriot et al., 2022). The statistical analysis between the PMW measurements and the SIT estimates are conducted for the ICESat-2 SIT (Petty et al., 2022), for the CS2SMOS SIT (Ricker et al., 2017), and for Nucleus for European Modelling of the Ocean (NEMO) (Madec & Team, 2008; Rousset et al., 2015) modeled SIT. The data and methodology are described

respectively in Sections 2 and 3. The machine-learning algorithm is trained on the ICESat-2 SIT. The results and their evaluations are presented in Section 4. Section 5 concludes this study.

2. Data

SMAP and AMSR2 provide brightness temperatures (T_B) from 1.4 GHz (L band) to 89.0 GHz (W band) that include the frequency range (1.4–36.5 GHz, from L to Ka bands) that will be observed by CIMR. The satellite-derived SIT are extracted from laser altimetry (ICESat-2) or from a combination of radar altimetry and low frequency PMW observations (CS2SMOS). The SIT from the NEMO model is also used. Comparisons are conducted with the IceBridge-QL aircraft campaign measurements (Kurtz, Richter-Menge et al., 2013).

All large-scale datasets are extracted over the Arctic Ocean above 55°N, for a complete polar year from 1 November 2018, to 31 October 2019. Data are projected onto the same EaseGrid 2.0 at ~12.5 km (Brodzik et al., 2012). The sea ice mask from Ocean and Sea Ice Satellite Application Facility (OSI-SAF) is adopted (Tonboe et al., 2017).

2.1. Passive Microwave Satellite Observations

2.1.1. SMAP

Since January 2015, the NASA SMAP mission observes the Earth at 1.4 GHz at both vertical (V) and horizontal (H) polarizations, from a Sun-synchronous 6 a.m./6 p.m. orbit (Entekhabi et al., 2014). It has a 6 m real aperture antenna that provides a spatial resolution of 40 km. The observing incidence angle is 40°, with a 1,000 km swath. Its orbit inclination angle of 98° allows the full coverage of the poles.

We use the daily surface T_B at 25 km spatial resolution from L2 product (Meissner et al., 2018) provided by Remote Sensing System (https://data.remss.com/smap/SSS/V05.0/FINAL/L2C last access: 9 March 2022). These T_B are corrected for the extra-terrestrial signal, and for the Faraday rotation.

2.1.2. AMSR2

AMSR2 is a radiometer on board the Japanese polar orbiting satellite GCOM-W, launched in May 2012. It provides observations at 55° incidence angles at 6.9, 7.3, 10.65, 18.7, 23.8, 36.5, and 89 GHz, at both V and H polarizations, with spatial resolution from 48 km at 6.9 GHz to 4 km at 89 GHz. With an inclination angle of 98.2°, AMSR2 does not observe the Arctic above 88°N. Here, we analyze the frequencies common to the CIMR instrument (noted 6, 10, 18, and 36 GHz hereafter). The Level-1R daily T_B at their native spatial resolution (Maeda et al., 2016) are obtained from the JAXA website (https://gportal.jaxa.jp, last access: 9 March 2022).

The EaseGrid 2.0 12.5 km spatial resolution is close to the 10 km spatial sampling of the AMSR2 observations, and to the spatial resolution at 36 GHz (Maeda et al., 2016). Within each grid cell, the SMAP and AMSR2 T_B are averaged on a ~10-day period (depending on the month, the last 10-day period in the month can be slightly longer or shorter), for each frequency, and polarization.

2.2. Satellite-Derived Sea Ice Thickness Over the Arctic

2.2.1. ICESat-2 SIT

The ICESat-2 L4 monthly SIT product (Petty et al., 2022) is available from https://nsidc.org/data/IS2SITMOGR4 (last access: 19 April 2022), on a 25 km grid, over the winter. It is based on the laser measurement of the total height of the freeboard (the thickness of the emerged sea ice layer plus the snow cover layer) if SIC is >50%, if height samples are at least 25 km off the coast, and under cloud-free conditions. Hydrostatic equilibrium is assumed for estimating the total SIT from the measured freeboard. Estimates of the snow depth as well as the snow, ice, and water densities are also required. The snow depth and density are simulated from the NASA Eulerian Snow on Sea Ice Model (NESOSIM v1.0) (Petty et al., 2018), modified with an empirical linear piecewise function to increase the initial model spatial resolution (Petty et al., 2020). The monthly data set has been duplicated for each of the three 10-day periods for each month. In addition, the data have been duplicated to fill the 12.5 km grid.

2.2.2. CS2SMOS SIT

The CS2SMOS SIT product combines the CS2 radar altimeter estimates (Hendricks et al., 2016; Ricker et al., 2014) with the PMW SMOS observations (Kaleschke et al., 2016; Tian-Kunze et al., 2014). The data can
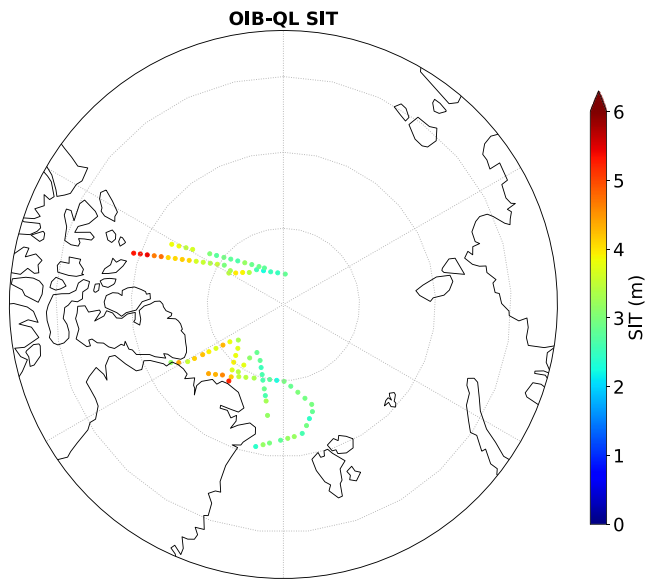
Figure 1. Sea Ice Thickness (SIT) as estimated from the Operation IceBridge QuickLook (OIB-QL) campaign data available for this study, in April 2019.

be found at ftps://smos-diss.eo.esa.int (last access: 19 April 2022). While CS2 lacks the capability to observe thin ice, SMOS retrievals are restricted to ice regimes thinner than ~1 m (Ricker et al., 2017).

Unlike ICESat-2, CS2 is considered to measure the ice-only freeboard, as the radar frequency (Ku-band at 13 GHz) is expected to penetrate the snow layer and reach the ice surface. Calculation of the total SIT relies on the hydrostatic equilibrium, with an estimate of the snow loading along with a snow, ice, and water density estimation. The CS2 SIT uses the snow climatology from Warren et al. (1999) for the snow depth and density. The original Warren climatological snow depth is reduced by 50% over first-year sea ice (Kurtz & Farrell, 2011), where discrimination between first-year and multi-year sea ice type is provided by the satellite-derived OSI-SAF product (Aaboe & Down, 2021). The method to retrieve the thin ice SIT from SMOS T_B at 1.4 GHz is based on a thermodynamic sea-ice model and a one-ice-layer radiative transfer model (Tian-Kunze et al., 2014).

An optimal interpolation scheme is developed to merge the CS2 and SMOS SIT estimates. It is applied to weekly CS2 and SMOS SIT estimates, allowing the estimation of the full SIT range. The product is available from mid-October to mid-April, on a 25 km grid. It is a weekly product available on a daily-basis. All the available observations acquired during this 10-day time-period are averaged for comparison with the other products. The values are duplicated to fill the common 12.5 km EASE grid.

2.3. NEMO Simulations

The NEMO model is a state-of-the-art modeling framework for research activities and forecasting services in ocean and climate sciences (Madec & Team, 2008). It uses the Louvain-La-Neuve Sea Ice Model 3.6 (LIM3.6) (Rousset et al., 2015).

In this study, the global high-resolution monitoring and forecasting system PSY4V3R1 (Gasparin et al., 2018) is adopted. It is based on version 3.1 of the NEMO/LIM model, which assimilates satellite SIC from the EUMETSAT/OSI-SAF. The PSY4V3R1 NEMO/LIM model provides a daily SIT estimation at 1/12° resolution that is averaged on the common 12.5 km EASE grid 2.0, for each 10-day periods. In the following, the PSY4V3R1 NEMO/LIM SIT outputs will be abreviated by NEMO SIT.

2.4. Sea Ice Thickness Measurement Campaigns

The Unified SIT Climate Data Record (Lindsay & Schweiger, 2013) aggregates all types of measurements of SIT from airplane and submarines operations, from 1947 to current time. In our time window (2018–2019), only the Operation IceBridge QuickLook (OIB-QL) data are available, and only at the end of the winter season (Kurtz, Farrell, et al., 2013). The measurements are provided by two instruments: first a 520 nm wavelength laser altimeter, the Airborne Topographic Mapper; second a nadir-looking frequency-modulated continuous-wave radar, the CReSIS snow radar. The SIT and its uncertainty are estimated from these two instruments, as explained in Kurtz, Farrell, et al. (2013).

In April 2019, 125,655 initial points have been measured and grouped to form 88 50-km clusters (Kurtz et al., 2012). Over the resulting 88 clusters collected by the OIB-QL campaign during this period, 78 are south of 88.5° and are collocated with the previously described datasets. The mean SIT value and its associated SIT uncertainty is provided for each cluster, and the mean SIT values are located on a map (Figure 1).

The 2018 OIB-Q data have also been extracted. It contains 200 clusters, acquired in April, and located in the same regions as for April 2019, with similar SIT distribution.

3. Method

3.1. Initial Analysis of the Data

Figure 2 shows, for the second 10-day period of November, January, and March, respectively, the SIT from ICESat-2, CS2SMOS, and NEMO as well as the V-polarized brightness temperature T_B^V at 1.4 GHz (SMAP) and
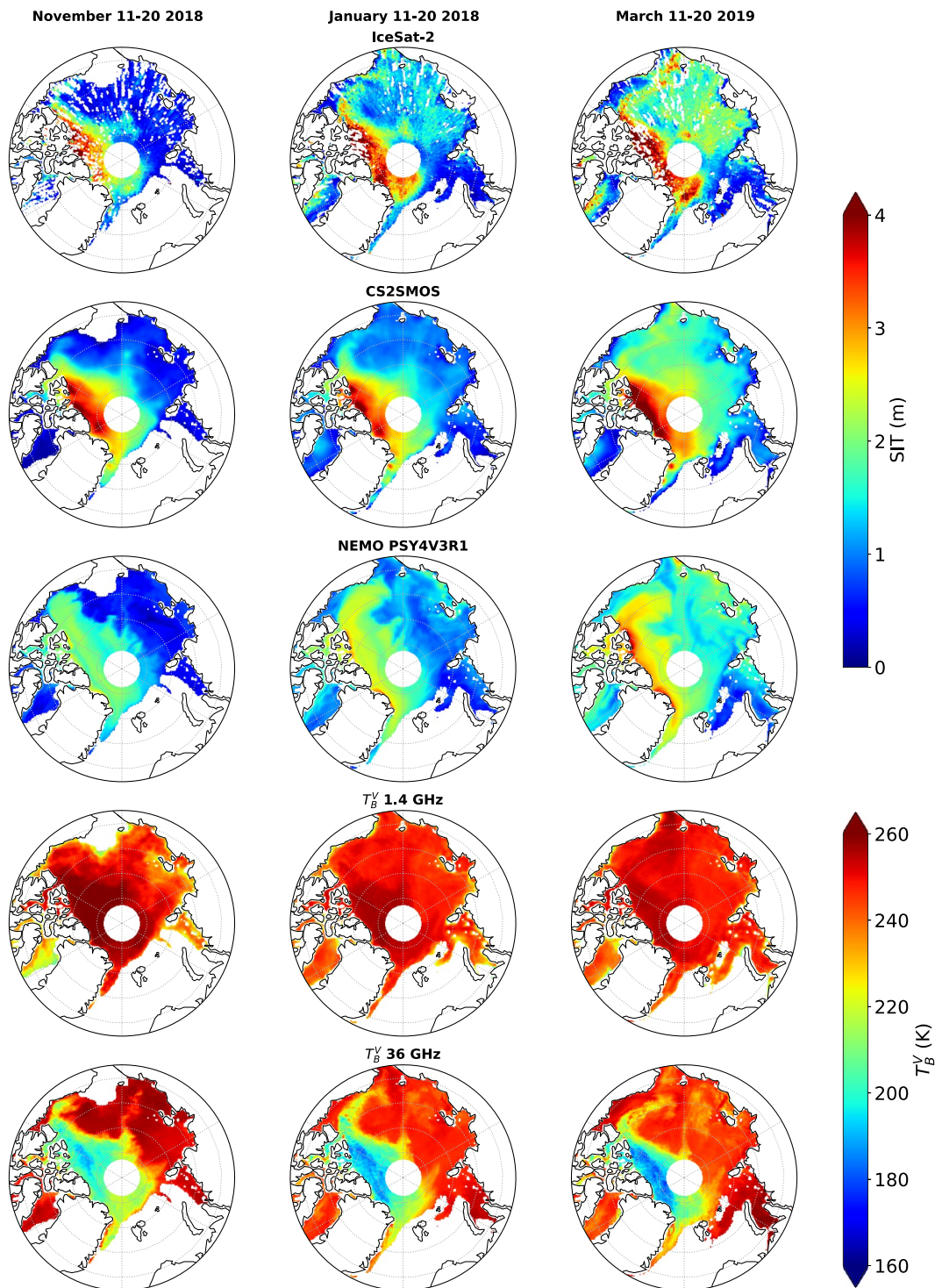

Figure 2. From top to bottom: ICESat-2 SIT, CS2SMOS SIT, NEMO SIT, SMAP T_B^V 1.4 GHz and AMSR2 T_B^V 36 GHz, for three 10-day winter periods (from left to right, the second 10-days periods in November 2018 January 2019, and March 2019), when SIC is above 0.8 (as provided by OSI-SAF estimates).

36 GHz (AMSR2), when the OSI-SAF SIC is above 0.8. SIT products from ICESat-2, CS2SMOS, and NEMO show similar broad spatial patterns, although NEMO exhibits significantly lower SIT north of Greenland and the Queen Elizabeth Islands than the satellite estimates. NEMO underestimates the large SIT compared to the other products, and CS2SMOS tends to show lower SIT than ICESAT-2 for these large SIT values as well. In these regions of high SIT, the sea ice emissivity at 1.4 GHz is high, and that translates in the maps into high T_B^V (>240 K), with a decrease of T_B^V in areas where sea ice is likely thin and transparent enough for the underneath ocean to contribute to the signal with its low emissivity. The T_B^V maps at 36 GHz exhibit spatial patterns negatively correlated with the SIT from the satellites, with a significant decrease of the T_B^V with increasing SIT.

To quantify theses spatial relationships, Figure 3 presents the linear correlation between the SIT from ICESat-2, CS2SMOS, and NEMO, as well as the correlation between the ICESat-2 SIT and T_B^V as a function of time during winter, for selected microwave channels. While the 1.4 GHz T_B^V shows limited correlation with the SIT and the 6 GHz T_B^V shows almost no correlation, there is a strong anti-correlation between the ICESat-2 SIT and T_B^V, at 18 and 36 GHz.

High negative correlation between T_B^V at 18 and 36 GHz and the other SIT products (CS2SMOS and NEMO) is also observed (not shown), with particularly high negative correlation between CS2SMOS and T_B^V at 18 and 36 GHz (above 0.9 in absolute value during the full winter). The spatial linear correlations have also been calculated for two SIT ranges, with a threshold at 0.7 m (not shown). For thin ice below 0.7 m, the correlation between T_B^V at 1.4 GHz and the CS2SMOS SIT is higher than with the other SIT products (ICESat-2 and NEMO). This behavior can be related to the use of T_B at 1.4 GHz in the CS2SMOS product, for its expected sensitivity to the thin ice thickness.

The physical interpretation of this anti-correlation between the T_B^V at higher frequencies and the SIT is not straightforward. Whereas some of these anti-correlations could partly been related by the temperature profile in the snow/ice system, these frequencies are not expected to sound within the snow and sea ice. A strong decrease of T_B with increasing frequency is a sign of scattering processes in the radiative transfer (Ulaby & Long, 2014). In these regions of low T_B at 18 and 36 GHz, the microwave signal is likely scattered, within the snow pack (volume scattering due to the formation of depth hoar for instance), at the snow surface and snow/sea ice interface (scattering over rough surfaces), and possibly within the sea ice (volume scattering in the desanilized multi-year sea ice). The microwave scattering signatures have been analyzed recently, using a state-of-the-art radiative transfer model to explore the co-variability of the microwave observations (passive and active) (Soriot et al., 2022). This study underlined the complexity of the scattering responses, and the difficulty to propose consistent and quantified explanations for all signatures, across frequencies. The regions with large scattering at 18 and 36 GHz also correspond to multi-year ice areas, where snow accumulates, where rafting and ridging occur, and where the sea ice has a low salinity. This scattering signal at 18 and 36 GHz has already been exploited to classify the sea ice types (e.g., Comiso, 1990; Lee et al., 2017). The relationship between T_B and SIT is likely indirect, but it is strong and, as a consequence, it can potentially be exploited for SIT estimation. Given the complexity of emission and scattering processes within the sea ice and snow pack, capitalizing on indirect relationships is already commonly done and these frequencies (namely 18 and 36 GHz) have been extensively used to estimate snow depth over sea ice as well as sea ice type, without a robust and clear physical explanation of the link between the observations and the snow and ice parameters of interest (see for instance Rostosky et al., 2018).

3.2. Statistical Inversion

Given the statistical relationships observed between T_B and SIT, a statistical inversion is tested, based on NN techniques. NNs have already been widely used in satellite remote sensing for the retrieval of a large number of geophysical parameters, including sea ice variables (Braakmann-Folgmann & Donlon, 2019; Chi & Kim, 2021; Rösel et al., 2012). Here we adopt a specific NN architecture called Multi Layered Perceptron (MLP) (Rumelhart et al., 1985). The MLP is appropriate to approximate multivariate non-linear mappings (Aires et al., 2002; Cybenko, 1989; Krasnopolsky, 2007), and will be applied here to build the statistical model reproducing the mapping
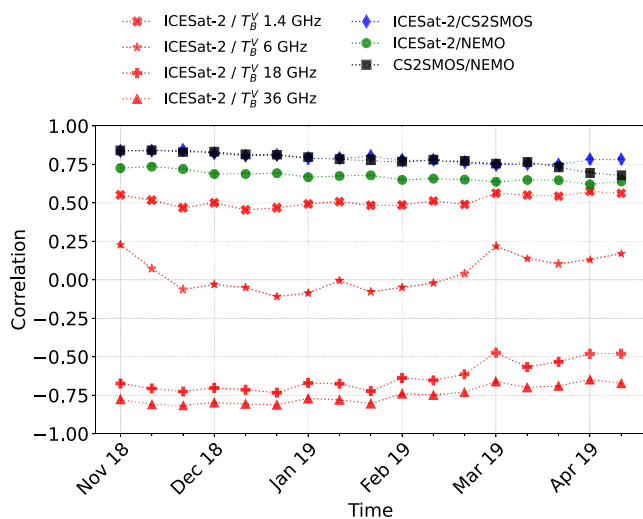

Figure 3. Spatial linear correlation among SIT and between ICESat-2 SIT and selected T_B (1.4, 6, 18, 36 GHz), as a function of time during winter in the Arctic, when SIC is above 0.8 (as provided by OSI-SAF estimates).

between brightness temperatures and SIT. The MLP will contain a first layer with as many input neurons as microwave channels used in the retrieval, followed by a hidden layer with hyperbolic tangent sigmoid activation functions, and an output layer with a linear activation function and one node outputting the retrieved SIT. This NN architecture can be represented by a function:

$$y = a_0 + \sum_{j=1}^{k} a_j \cdot \tanh \left(b_{j0} + \sum_{i=1}^{n} b_{ji} \cdot x_i \right);$$ (1)

where x_i are components of the NN input vector, y is the single NN output, a and b are the matrices of the fitting parameters, that is, the NN weights and biases, n is the number of inputs, k is the number of nodes in the hidden layer, and tanh is the hyperbolic tangent sigmoid activation function. The parameters a and b are determined during the training phase using a database of T_B and corresponding SIT, together with the training algorithm of Foresee and Hagan ([1997]). To decide on the k number of nodes, NNs with increasing k are tested till the NN prediction error stabilizes, an indication that no further improvements on the NN prediction can be gained by making the NN more complex. To avoid spatial or temporal overfitting and increase the robustness of the retrieval, only a random third of the database is used for the training, as in Rodríguez-Fernández et al. ([2019]), and an early-stop validation technique is applied during the training (Prechelt, [2012]).

The NN is trained on the ICESat-2 SIT, to prevent the inbreeding with the PMW T_B inputs if using CS2SMOS. The ICESat-2 SIT is expected to be independent of PMW observations (Petty et al., [2020]) and is retrieved from a different frequency domain (visible vs. microwave) (Abdalati et al., [2010]). Indeed, the CS2SMOS product is constructed with T_B at 1.4 GHz from SMOS (Ricker et al., [2017]), and the NEMO model assimilates OSI-SAF SIC which is based on microwave T_B. However, similar exercise could be performed with a NN trained on CS2SMOS or NEMO. In order to minimize the SIC influence, the NN is trained on pixels with SIC > 0.8, as estimated from OSI-SAF.

Several combinations of brightness temperatures have been tested as inputs to the NN and the results are compared with the SIT estimates from CS2SMOS, NEMO, and OIB-QL. Among the tested T_B combinations, two are particularly interesting for further studies: the combination of all CIMR frequencies (1.4, 6, 10, 18, and 36 GHz at both V and H polarizations) to showcase the future capability of CIMR to estimate SIT, and the combination of only 18 and 36 GHz V and H channels, to facilitate the production of long time series of SIT (because of the availability of long-time records of these observations, with SSM/I, its successor SSMIS, and possibly its ancestor, the Scanning Multichannel Microwave Radiometer (SMMR)).

4. Results and Discussion

4.1. Global Arctic Results Over the Winter

First, a NN inversion is trained on a subset of the ICESat-2 SIT product, using all the frequencies from the CIMR-like database, from 1.4 to 36 GHz (named PMW$_{CIMR}$ hereinafter). Over the Arctic winter, the linear correlation between the retrieved SIT and the ICESat-2 product is 0.85, with a root mean square difference (RMSD) of 0.54 m.

Figure [4] shows some statistical analyses comparing the different SIT products, including the PMW$_{CIMR}$ retrieval: the spatial linear correlation between the different SIT products as a function of the time (top panel), the RMSD between the different products and the PMW$_{CIMR}$ retrieval as a function of

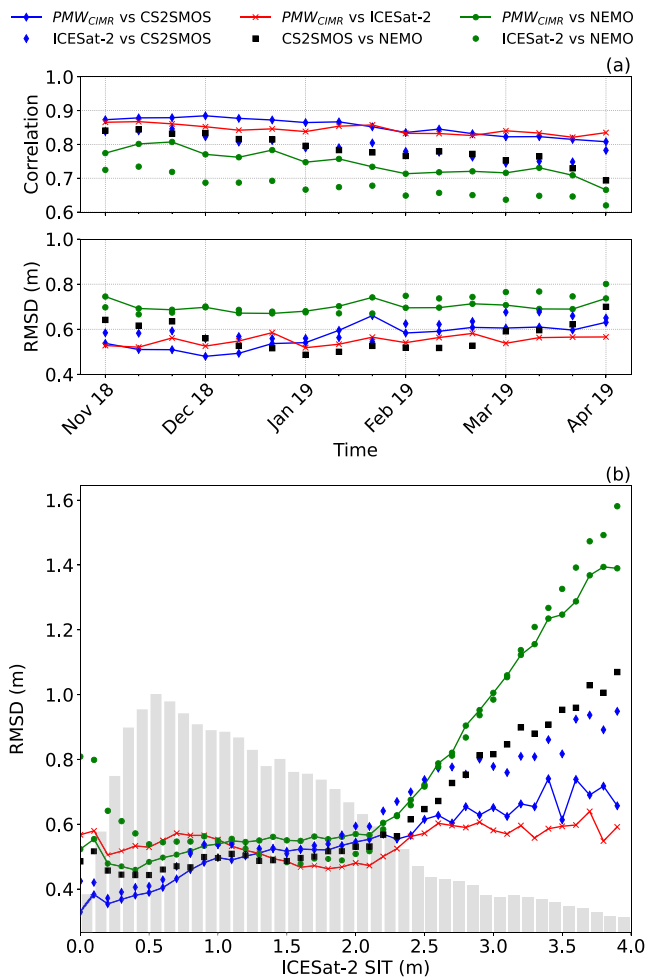**Figure 4.** Statistics for inter-product differences, including the PMW$_{CIMR}$ retrieval. Top: Spatial linear correlation (R) between PMW$_{CIMR}$ estimates as a function of time in the winter. Middle: RMSD in m between the variables, also as a function of time in the winter. Bottom: the RMSD between the SIT estimates, as a function of the ICESat-2 SIT (with the ICESat-2 SIT distribution indicated in gray shades).

time (middle panel), or as a function of the ICESat-2 SIT (bottom panel). The normalized distribution of the ICESat-2 SIT is also shown in gray shades on the bottom panel.

The general agreement between the satellite products ICESat-2 and CS2SMOS is better (both in terms of spatial correlation and RMSD) than between the satellite products and the NEMO SIT estimates (Figure 4 top panels), as already expected from Figure 2. The agreements are rather stable during the winter, with a slight degradation (decreased correlation and increased RMSD) at the end of the winter season (Figure 4 two top panels). The PMW_{CIMR} retrieval shows better spatial correlation and smaller RMSD with all SIT products at each time step (Figure 4 two top panels, symbols with solid lines), as compared to the correlation and RMSD between the ICESat-2 original product and the other SIT products (Figure 4 two top panels, symbols without solid lines). Note that the spatial correlation between PMW_{CIMR} and CS2SMOS SIT is even higher than the correlation between PMW_{CIMR} SIT and the original ICESat-2 SIT used to train it, meaning that the PMW information in the PMW_{CIMR} retrieval adds to the agreement between the existing SIT estimates.

The RMSD between products tend to significantly increase between most products, for SIT above ∼2 m (Figure 4 bottom panel). The SIT population above 2 m is rather limited for all SIT products (the ICESat-2 SIT distribution is indicated in gray shades on Figure 4). For the full SIT range, and especially for the lower and higher SIT, the RMSD between the PMW_{CIMR} retrieval and the other products decreases (symbols with solid lines on Figure 4 bottom panel) as compared to the initial RMSD between ICESat-2 and the other products (symbols without solid lines on the same panel).

Figure 5 shows the maps of the PMW_{CIMR} SIT and the difference between its estimates and the ICESat-2-based SIT estimates for three different 10-day winter periods (11/2018, 01/2019, and 04/2019) not used in the NN training. The maps of the ICESat-2 SIT were already shown (Figure 2). The PMW_{CIMR} SIT maps show the same general patterns as seen in Figure 2, with high SIT north of Greenland and in the Canada Basin, with an increase of the SIT over the winter in the Chukchi Sea. Noticeable differences between PMW_{CIMR} and ICESat-2 SIT are located along the east coast of Greenland, especially in January, where PMW_{CIMR} exhibits higher SIT values than ICESat-2. In this region, note that both CS2SMOS and NEMO have SIT larger than the initial ICESat-2, and closer to the PMW_{CIMR} retrieval (Figure 2). North of the islands of Franz Joseph Land, especially in March, the PMW_{CIMR} predicts higher SIT than ICESAT-2, where also both CS2SMOS and NEMO have higher SIT than
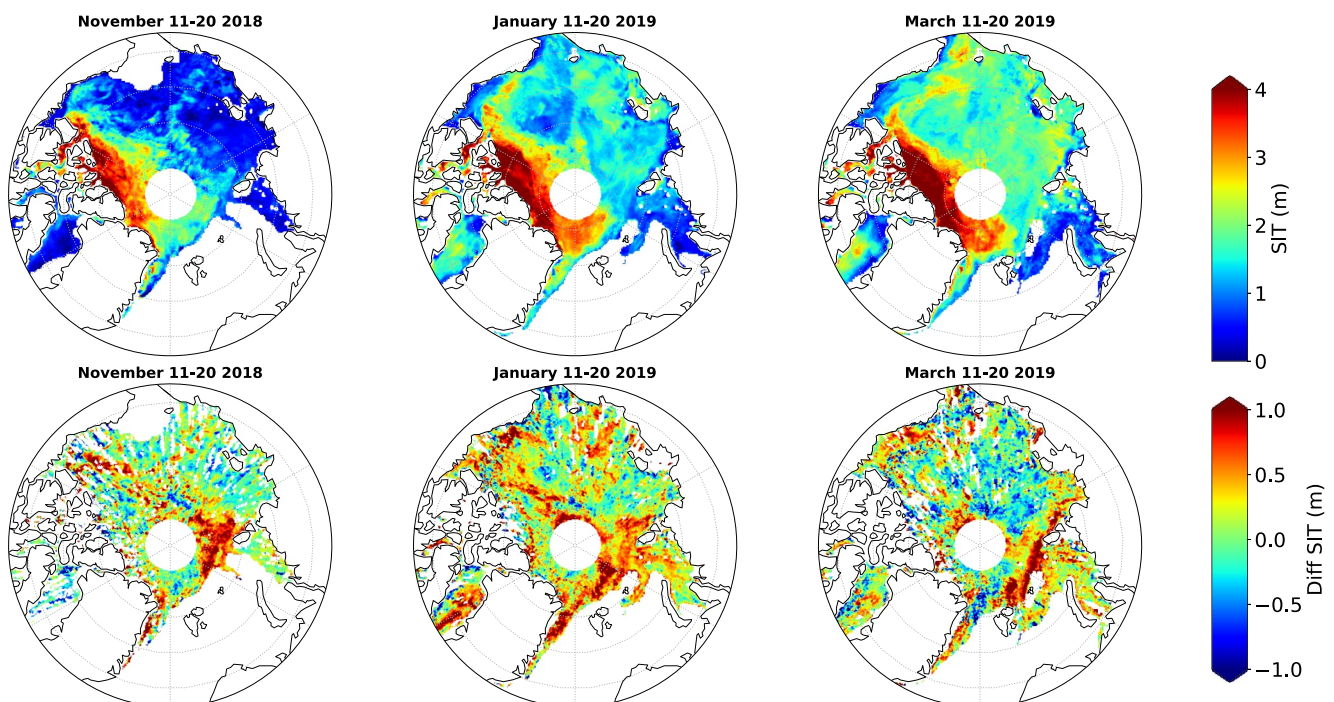

Figure 5. From top to bottom: maps of PMW_{CIMR} SIT, and PMW_{CIMR} SIT minus ICESat-2 SIT, for the PMW_{CIMR} retrieval. For 10-days periods in November 2018 (left), January 2019 (center), and April 2019 (right).
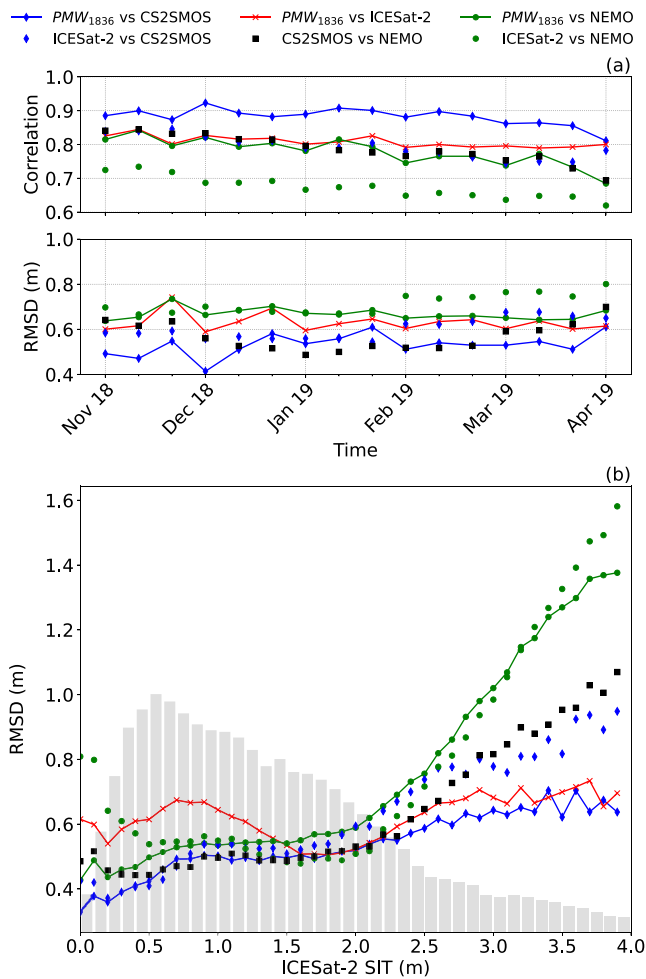
Figure 6. Same as Figure 4, but using the PMW$_{1836}$ retrieval instead of PMW$_{CIMR}$.

ICESat-2. On the contrary, PMW$_{CIMR}$ shows thinner SIT than ICESat-2, in the Bering Strait in January.

The SIT retrieval has also been tested using less frequencies in the training of the NN. Suppressing only the 1.4 GHz channels in the NN does not change much the results (not shown): the correlation with ICESat-2 over the full winter decreases from 0.85 to 0.83, and the RMSD increases from 0.54 to 0.57 m. It tends to slightly degrade the retrieval of small SIT (<1 m), as compared to the original ICESAT-2 SIT (RMSD from 0.57 to 0.58 m), and to the CS2SMOS SIT (RMSD from 0.42 to 0.45 m), as expected.

Tests are then performed using only the 18 and 36 GHz channels (both V and H polarizations), named PMW$_{1836}$ hereinafter. With this combination, longer SIT time series could be produced, using previous radiometers such as SSM/I (launched in 1987), its successors SSMIS, or even SMMR (launched in 1978) that all include the 18 and 36 GHz channels. The results are presented in Figure 6. The correlation between PMW$_{1836}$ and ICESat-2 SIT decreases over the full winter (from 0.85 with all channels to 0.80 using only 18 and 36 GHz channels), and the RMSD increases (from 0.54 to 0.62 m), suggesting that the retrieval using only two frequencies would slightly degrade the SIT results compared to the use of all the frequencies available on CIMR, at least when considering ICESat-2 as the reference.

However, surprisingly, compared to CS2SMOS, the correlation and the RMSD do not change much when using all frequencies or 18 and 36 GHz only, with even a slight increase of the correlation (from 0.85 with the CIMR frequencies to 0.88 with only the 18 and 36 GHz channels) and a decrease of the RMSD when suppressing all the lower frequencies (from 0.58 m with the CIMR frequencies to 0.54 m with only the 18 and 36 GHz). An explanation could be related to the use of the PMW 18 and 36 GHz channels in the CS2SMOS retrieval, for adjusting the snow depth. Indeed, the CS2 altimeter data processing involves passive microwaves T_B at 18 and 36 GHz to modify the original Warren (Warren et al., 1999) snow depth climatology, following the Kurtz and Farrell (2011) method. To overcome the need for external snow depth information, future altimeters such as CRISTAL (Kern et al., 2020) will be equipped with dual-frequency radar altimeters, with the snow depth estimation being derived from the difference between the signals at Ku (13 GHz) and Ka (35 GHz) frequencies. Garnier et al. (2021) already tested this possibility for snow depth and SIT retrievals with encouraging results, using two different altimetric missions, CS2 at 13 GHz and SARAL/AltiKa at 35 GHz (Verron et al., 2015). With SARAL/AltiKa limited to 82°N (thus excluding most of the multi-year ice), we did not consider this product in the current comparison.

To further explore the skills of the PMW retrievals, Table 1 shows the spatio-temporal Pearson correlation between the different SIT products, for three SIT ranges: 0–1 m, 1–2 m, and >2 m. The SIT ranges are based on the ICESat-2 product. The correlations between PMW$_{CIMR}$ or PMW$_{1836}$ and ICESat-2 SIT products are similar to the correlations between the two official ICESat-2 and CS2SMOS products, for all SIT ranges. Note that for each SIT range, the correlation between PMW$_{CIMR}$ or PMW$_{1836}$ and CS2SMOS is significantly higher than the correlation between ICESat-2 and CS2SMOS SIT.

The methodology and its results described here differs from what have been done before (Chi & Kim, 2021) in several ways. First, in preparation for the CIMR mission, we use only the channels that will be available on that mission (1.4, 6, 10, 18, and 36 GHz). Second, we train our NN on a data set

Table 1

Spatio-Temporal Correlation Between the Different Satellite-Based SIT Products, Including PMW$_{CIMR}$ and PMW$_{1836}$, for Different Sea Ice Thickness Ranges

	0–1 m	1–2 m	+2 m
ICESat-2/CS2SMOS	0.46	0.33	0.56
ICESat-2/PMW$_{CIMR}$	0.44	0.39	0.71
ICESat-2/PMW$_{1836}$	0.45	0.33	0.63
CS2SMOS/PMW$_{CIMR}$	0.65	0.57	0.77
CS2SMOS/PMW$_{1836}$	0.69	0.66	0.80

Note. The SIT from ICESat-2 is used as reference, to sort the SIT ranges.
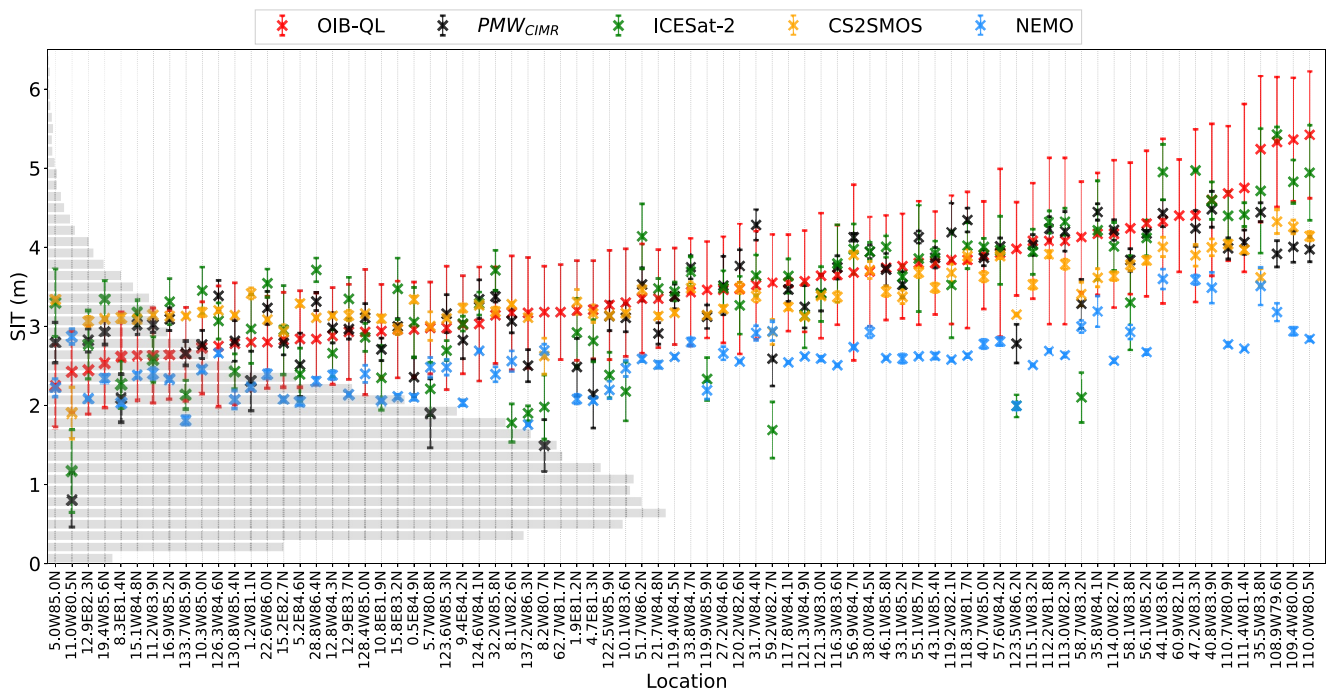
Figure 7. Comparison of SIT measurements from OIB-QL (red), PMW$_{CIMR}$ retrieval (black), ICESat-2 (green), CS2SMOS (orange) and NEMO (blue) products. The error bars represent the mean SIT uncertainty for OIB-QL measurements and one standard deviation for the other SIT estimations. The normalized distribution of the ICESat-2 SIT is shown in gray shades on the left *y*-axis.

that is completely independent of the microwave observations (ICESat-2). Finally, we use a simple yet robust and efficient NN architecture (MLP) that is already used for other geophysical retrievals (Jimenez et al., 2009; Prigent & Jimenez, 2021), and that is sufficient for this kind of problem. We tested different NN structures, and complexifying the initial NN was clearly not necessary.

4.2. Evaluation With the OIB-QL Campaign Measurements

The PMW$_{CIMR}$ estimates are now evaluated with the OIB-QL campaign measurements in April 2019. Figure 7 shows the results of the comparison between the OIB-QL SIT measurements with the satellite and model retrievals, including the NN retrieval PMW$_{CIMR}$ using all the frequencies from 1.4 to 36 GHz. The clusters were organized by increasing OIB-QL SIT measurement, and their location is provided for each cluster. For each OIB-QL cluster, the mean OIB-QL SIT is shown with its associated uncertainty (red crosses and error bars). For the same clusters, the mean SIT retrieved (crosses) and their associated standard deviation (error bars) are shown for PMW$_{CIMR}$ in black, ICESat-2 in green, CS2SMOS in orange and the NEMO model in blue. The normalized distribution of the ICESat-2 SIT is also shown in gray shades.

The range of SIT measured by the OIB-QL campaign shows that most of the observed sea ice is multi-year, with the OIB-QL values in the high tail of the distribution of the ICESat-2 SIT. The mean SIT measured by the OIB-QL campaign is 3.4 m with a standard deviation of 0.72 m. CS2SMOS and NEMO show small range of SIT, which can be explained by the fact that these products are spatially smooth (see Figure 2), with consequently limited variations over a flight. The NEMO model tends to systematically underestimate the SIT, compared to the measurements campaign, as well as compared to the satellite retrievals.

Table 2 presents statistics between the OIB-QL SIT and the others SIT retrievals (including PMW$_{1836}$). PMW$_{CIMR}$ shows rather good agreement with

Table 2
Bias, Standard Deviation, Root-Mean-Square Difference, Relative Root-Mean-Square Difference, and Pearson Correlation Coefficient Between the OIB-QL SIT and the Other SIT Retrievals for the Polar Winter 2018–2019

	Mean Difference (m)	STD (m)	RMSD (m)	Relative RMSD (%)	*R*
PMW$_{CIMR}$	0.16	0.55	0.57	17	0.72
PMW$_{1836}$	0.28	0.55	0.61	18	0.74
IS2	0.17	0.64	0.66	20	0.69
CS2SMOS	0.11	0.47	0.49	14	0.80
NEMO	0.94	0.54	1.09	28	0.69

Table 3
Bias, Standard Deviation, Root-Mean-Square Difference, Relative Root-Mean-Square Difference, and Pearson Correlation Coefficient Between the OIB-QL SIT and the Other SIT Retrievals for the Polar Winter 2017–2018

	Mean Difference (m)	STD (m)	RMSD (m)	Relative RMSD (%)	R
PMW_{CIMR}	−0.08	0.49	0.50	27	0.78
PMW_{1836}	−0.17	0.56	0.59	34	0.69
CS2SMOS	0.04	0.49	0.49	24	0.76

the OIB-QL measurements with linear correlations of 0.72, a bias of 16 cm, and a RMSD of 57 cm. The differences between PMW_{CIMR} and PMW_{1836} results are rather limited, considering that 10 channels are used in the first algorithm and only 4 in the second. The CS2SMOS SIT product shows the best agreements with OIB-QL measurements with low mean bias of 11 cm, a RMSD of 49 cm, and a high correlation of 0.8. The PMW_{CIMR} SIT performs slightly better than the ICESat-2 product. NEMO tends to underestimate the OIB-QL values, with a mean bias nearly three times higher than the next worst result (PMW_{1836}), and a RMSD almost two times larger than the other products.

The SIT distribution of the OIB-QL mission is heavily weighted toward very high SIT values (mainly above 3 m) representing mostly multi-year ice. That does not correspond to the whole Arctic SIT distribution, where first-year ice with lower SIT are dominating (see the gray shades in Figure 4). The conclusions drawn from the OIB-QL based evaluation cannot be extended to the validity and quality of the estimates for low SIT. Note that in the SIT range measured by the OIB-QL campaign (mainly above 3 m), the PMW retrieval errors with respect to the other satellite products (ICESat-2 or CS2SMOS) were expected to have RMSD ~0.6 m (see Figures 4 and 6). The whole Arctic basin having more thin ice where PMW_{CIMR} is expected to perform well (see Figure 4), scores might even be better than Table 2 indicates.

In order to further evaluate the algorithms for another winter not used in the training, the OIB-QL SIT acquired during the polar winter 2017–2018 have been compared to the PWM retrievals, as well as with the CS2SMOS estimates (note that ICESat-2 was not launched yet). The statistics are presented in Table 3. The results show very similar performances for that winter than for the 2018–2019 winter, showing the robustness of our retrievals to the inter-annual variability. With the Operation IceBridge (OIB) measurements targeting the same region and the same period of the year for all years, the SIT distribution from these measurements is similar over the available years.

5. Conclusion

A simple and yet efficient statistical approach is developed to estimate the SIT from PMW T_B between 1.4 and 36 GHz. It is based on the evidence of high absolute correlations between the observed PMW brightness temperatures (especially at 36 GHz) and existing available satellite-derived SIT products. The 1.4–36 GHz frequency range will be covered by the future CIMR mission to be launched by the end of the 2020s. Using a combination of SMAP and AMSR2 observations, a NN inversion is trained on a subset of ICESat-2 SIT product derived from independent laser-altimeter measurements, and the PMW SIT is estimated over the Arctic for a full winter season.

The resulting PMW SIT using all CIMR frequencies shows a significant correlation with the ICESat-2 SIT data during the whole Arctic winter (0.85 on average, Figure 4) and an identical spatio-temporal correlation with the CS2SMOS SIT product (0.85). The PMW inversion using only the 18 and 36 GHz frequencies also performs satisfactorily, over the full SIT range, but with slightly lower correlation (Figure 6). That will make it possible to calculate long time series of SIT from former PMW imagers such as SSM/I and SSMIS back to the end of the 80s, or even from SMMR, launched in 1978, with all these instruments being equipped with radiometers at 18 and 36 GHz, at both V and H polarizations. Note that there are on-going efforts to inter-calibrate all these microwave imagers for climate purposes, and this SIT estimation could benefit from this very long record of high quality T_B at 18 and 36 GHz (Fennig et al., 2020).

The PMW retrievals were compared to OIB-QL measurement campaigns performed in 2018 and 2019. Both PMW retrievals (with all frequencies and with 18 and 36 GHz only) show encouraging performances, comparable to the results obtained with the current ICESat-2 or CS2SMOS SIT products, at least for the SIT range covered by the OIB-QL measurements (mainly above 3 m).

Several satellite-based SIT exist, each with limitations due to their operating frequency or their algorithm assumptions. The CS2SMOS and ICESat-2 SIT products both require a characterization of the snow cover (snow depth and snow density). The use of dual frequency (Ku/Ka) radar altimeters (as in Kwok et al. (2020) or Garnier et al. (2021)) can help reduce the uncertainties related to the snow depth, and the future CRISTAL mission, to be

launched approximately at the same time as CIMR, will be equipped with this dual frequency capability (Kern et al., 2020). The PMW SIT retrieval proposed here is based on a pragmatic approach. It does not require any ancillary information. It is easy to apply on past, current, or future observations, providing close-to panarctic coverage, sub-monthly, over long time records.

Data Availability Statement

The SMAP brightness temperatures used for mimicking the 1.4 GHz CIMR channel in the study are available at www.remss.com. The AMSR2 brightness temperatures used for mimicking the other CIMR channels in the study are provided by Japan Aerospace Exploration Agency available at https://gportal.jaxa.jp/. The ICESat-2 L4 monthly SIT product used in this study is provided by the National Snow and Ice Data Center, available at https://nsidc.org/data/is2sitmogr4/versions/2 (last access 19 April 2022) (Petty et al., 2022). The production of the merged CryoSat-SMOS SIT data, used in this study, was funded by the ESA project SMOS & CryoSat-2 Sea Ice Data Product Processing and Dissemination Service, and data from 19 April 2022 (Ricker et al., 2017). The NEMO PSY4V3R1 SIT data used in this study is provided by MERCATOR and available at https://datastore.cls.fr/catalogues/mercator-model-psy4v3-velocity-112/. The Operation Ice Bridge QuickLook (Kurtz, Richter-Menge et al., 2013) data used in this study is provided by the National Snow and Ice Data Center and available at http://psc.apl.uw.edu/sea_ice_cdr/Sources/IceBridge-QL.html (last access 19 April 2022). The CIMR-like database construct with the mentioned instrument can be found on the Figshare website with the following https://doi.org/10.6084/m9.figshare.21494100.

References

Aaboe, S., & Down, E. J. (2021). Product user manual for the global sea-ice edge and type product (Tech. Rep.).

Abdalati, W., Zwally, H. J., Bindschadler, R., Csatho, B., Farrell, S. L., Fricker, H. A., et al. (2010). The ICESat-2 laser altimetry mission. *Proceedings of the IEEE*, *98*(5), 735–751. https://doi.org/10.1109/JPROC.2009.2034765

Abdalla, S., Abdeh Kolahchi, A., Ablain, M., Adusumilli, S., Aich Bhowmick, S., Alou-Font, E., et al. (2021). Altimetry for the future: Building on 25 years of progress. *Advances in Space Research*, *68*(2), 319–363. https://doi.org/10.1016/j.asr.2021.01.022

Aires, F., Chédin, A., Scott, N. A., & Rossow, W. B. (2002). A regularized neural net approach for retrieval of atmospheric and surface temperatures with the IASI instrument. *Journal of Applied Meteorology and Climatology*, *41*(2), 144–159. https://doi.org/10.1175/1520-0450(2002)041<0144:arnnaf>2.0.co;2

Braakmann-Folgmann, A., & Donlon, C. (2019). Estimating snow depth on Arctic sea ice using satellite microwave radiometry and a neural network. *The Cryosphere*, *13*(9), 2421–2438. https://doi.org/10.5194/tc-13-2421-2019

Brodzik, M. J., Billingsley, B., Haran, T., Raup, B., & Savoie, M. H. (2012). EASE-Grid 2.0: Incremental but significant improvements for earth-gridded data sets. *ISPRS International Journal of Geo-Information*, *1*(1), 32–45. https://doi.org/10.3390/ijgi1010032

Chi, J., & Kim, H.-C. (2021). Retrieval of daily sea ice thickness from AMSR2 passive microwave data using ensemble convolutional neural networks. *GIScience and Remote Sensing*, *58*(6), 812–830. https://doi.org/10.1080/15481603.2021.1943213

Comiso, J. C. (1986). Characteristics of Arctic winter sea ice from satellite multispectral microwave observations. *Journal of Geophysical Research*, *91*(C1), 975–994. https://doi.org/10.1029/JC091iC01p00975

Comiso, J. C. (1990). Arctic multiyear ice classification and summer ice cover using passive microwave satellite data. *Journal of Geophysical Research*, *95*(C8), 13411–13422. https://doi.org/10.1029/JC095iC08p13411

Comiso, J. C. (1995). SSM/I sea ice concentrations using the bootstrap algorithm (Vol. *53*).

Comiso, J. C., Cavalieri, D. J., & Markus, T. (2003). Sea ice concentration, ice temperature, and snow depth using AMSR-E data. *IEEE Transactions on Geoscience and Remote Sensing*, *41*(2), 243–252. https://doi.org/10.1109/TGRS.2002.808317

Connor, L. N., Laxon, S. W., Ridout, A. L., Krabill, W. B., & McAdoo, D. C. (2009). Comparison of Envisat radar and airborne laser altimeter measurements over Arctic sea ice. *Remote Sensing of Environment*, *113*(3), 563–570. https://doi.org/10.1016/j.rse.2008.10.015

Cybenko, G. (1989). Approximation by superpositions of a sigmoidal function. *Mathematics of Control, Signals and Systems*, *2*(4), 303–314. https://doi.org/10.1007/BF02551274

Dai, A., Luo, D., Song, M., & Liu, J. (2019). Arctic amplification is caused by sea-ice loss under increasing CO_2. *Nature Communications*, *10*(1), 121. https://doi.org/10.1038/s41467-018-07954-9

Donlon, C. (2020). CIMR mission requirements document v3 |cimr.eu (Tech. Rep. No. 4). Retrieved from https://cimr.eu/mrd_v3

Entekhabi, D., Njoku, E. G., O'Neill, P. E., Kellogg, K. H., Crow, W. T., Edelstein, W. N., et al. (2010). The soil moisture active passive (SMAP) mission. *Proceedings of the IEEE*, *98*(5), 704–716. https://doi.org/10.1109/JPROC.2010.2043918

Entekhabi, D., Yuech, S., & De Lannoy, G. (2014). *SMAP handbook*. JPL Publication.

Fennig, K., Schröder, M., Andersson, A., & Hollmann, R. (2020). A fundamental climate data record of SMMR, SSM/I, and SSMIS brightness temperatures. *Earth System Science Data*, *12*(1), 647–681. https://doi.org/10.5194/essd-12-647-2020

Font, J., Camps, A., Borges, A., Martín-Neira, M., Boutin, J., Reul, N., et al. (2010). SMOS: The challenging sea surface salinity measurement from space. *Proceedings of the IEEE*, *98*(5), 649–665. https://doi.org/10.1109/JPROC.2009.2033096

Foresee, F. D., & Hagan, M. T. (1997). Gauss-Newton approximation to Bayesian regularization. In *Proceedings of the 1997 international joint conference on neural networks* (pp. 1930–1935).

Garnier, F., Fleury, S., Garric, G., Bouffard, J., Tsamados, M., Laforge, A., et al. (2021). Advances in altimetric snow depth estimates using bi-frequency SARAL and CryoSat-2 Ka–Ku measurements. *The Cryosphere*, *15*(12), 5483–5512. https://doi.org/10.5194/tc-15-5483-2021

Gasparin, F., Greiner, E., Lellouche, J.-M., Legalloudec, O., Garric, G., Drillet, Y., et al. (2018). A large-scale view of oceanic variability from 2007 to 2015 in the global high resolution monitoring and forecasting system at Mercator Océan. *Journal of Marine Systems*, *187*, 260–276. https://doi.org/10.1016/j.jmarsys.2018.06.015

Hendricks, S., Ricker, R., & Helm, V. (2016). *User guide—AWI CryoSat-2 sea ice thickness data product* (v1.2). Retrieved from https://epic.awi.de/id/eprint/41242/1/AWI_cryosat2_user_guide_v1_2_july2016.pdf

Heygster, G., Huntemann, M., Ivanova, N., Saldo, R., & Pedersen, L. T. (2014). Response of passive microwave sea ice concentration algorithms to thin ice. In *2014 IEEE geoscience and remote sensing symposium* (pp. 3618–3621). IEEE. https://doi.org/10.1109/IGARSS.2014.6947266

Imaoka, K., Maeda, T., Kachi, M., Kasahara, M., Ito, N., & Nakagawa, K. (2012). Status of AMSR2 instrument on GCOM-W1. In *Earth observing missions and sensors: Development, implementation, and characterization II* (Vol. 8528, pp. 201–206). SPIE.

Jiménez, C., Prigent, C., & Aires, F. (2009). Toward an estimation of global land surface heat fluxes from multisatellite observations. *Journal of Geophysical Research*, *114*(D6). https://doi.org/10.1029/2008jd011392

Kaleschke, L., Tian-Kunze, X., Maaß, N., Beitsch, A., Wernecke, A., Miernecki, M., et al. (2016). SMOS sea ice product: Operational application and validation in the Barents Sea marginal ice zone. *Remote Sensing of Environment*, *180*, 264–273. https://doi.org/10.1016/j.rse.2016.03.009

Kashiwase, H., Ohshima, K. I., Nakata, K., & Tamura, T. (2021). Improved SSM/I thin ice algorithm with ice type discrimination in coastal polynyas. *Journal of Atmospheric and Oceanic Technology*, *38*(4), 823–835. https://doi.org/10.1175/JTECH-D-20-0145.1

Kern, M., Cullen, R., Berruti, B., Bouffard, J., Casal, T., Drinkwater, M. R., et al. (2020). The Copernicus polar ice and snow topography altimeter (CRISTAL) high-priority candidate mission. *The Cryosphere*, *14*(7), 2235–2251. https://doi.org/10.5194/tc-14-2235-2020

Kilic, L., Prigent, C., Aires, F., Boutin, J., Heygster, G., Tonboe, R. T., et al. (2018). Expected performances of the Copernicus imaging microwave radiometer (CIMR) for an all-weather and high spatial resolution estimation of ocean and sea ice parameters. *Journal of Geophysical Research: Oceans*, *123*(10), 7564–7580. https://doi.org/10.1029/2018JC014408

Krasnopolsky, V. M. (2007). Neural network emulations for complex multidimensional geophysical mappings: Applications of neural network techniques to atmospheric and oceanic satellite retrievals and numerical modeling. *Reviews of Geophysics*, *45*(3), RG3009. https://doi.org/10.1029/2006RG000200

Kurtz, N. T., & Farrell, S. L. (2011). Large-scale surveys of snow depth on Arctic sea ice from Operation IceBridge. *Geophysical Research Letters*, *38*(20), L20505. https://doi.org/10.1029/2011GL049216

Kurtz, N. T., Farrell, S. L., Studinger, M., Galin, N., Harbeck, J. P., Lindsay, R., et al. (2013). Sea ice thickness, freeboard, and snow depth products from Operation IceBridge airborne data. *The Cryosphere*, *7*(4), 1035–1056. https://doi.org/10.5194/tc-7-1035-2013

Kurtz, N. T., Richter-Menge, J., Farrell, S., Studinger, M., Paden, J., Sonntag, J., & Yungel, J. (2013). IceBridge airborne survey data support arctic sea ice predictions. *Eos, Transactions American Geophysical Union*, *94*(4), 41. https://doi.org/10.1002/2013EO040001

Kurtz, N. T., Studinger, M., Harbeck, J., Onana, V.-D.-P., & Farrell, S. (2012). *IceBridge sea ice freeboard, snow depth, and thickness*. NASA Distributed Active Archive Center at the National Snow and Ice Data Center. Retrieved from http://nsidc.org/data/idcsi2.html

Kwok, R. (2018). Arctic sea ice thickness, volume, and multiyear ice coverage: Losses and coupled variability (1958–2018). *Environmental Research Letters*, *13*(10), 105005. https://doi.org/10.1088/1748-9326/aae3ec

Kwok, R., Kacimi, S., Webster, M. A., Kurtz, N. T., & Petty, A. A. (2020). Arctic snow depth and sea ice thickness from ICESat-2 and CryoSat-2 freeboards: A first examination. *Journal of Geophysical Research: Oceans*, *125*(3), e2019JC016008. https://doi.org/10.1029/2019JC016008

Lavergne, T., Sørensen, A. M., Kern, S., Tonboe, R., Notz, D., Aaboe, S., et al. (2019). Version 2 of the EUMETSAT OSI SAF and ESA CCI sea-ice concentration climate data records. *The Cryosphere*, *13*(1), 49–78. https://doi.org/10.5194/tc-13-49-2019

Laxon, S., Peacock, N., & Smith, D. (2003). High interannual variability of sea ice thickness in the Arctic region. *Nature*, *425*(6961), 947–950. https://doi.org/10.1038/nature02050

Laxon, S. W., Giles, K. A., Ridout, A. L., Wingham, D. J., Willatt, R., Cullen, R., et al. (2013). CryoSat-2 estimates of Arctic sea ice thickness and volume. *Geophysical Research Letters*, *40*(4), 732–737. https://doi.org/10.1002/grl.50193

Lee, S.-M., Meier, W. N., Sohn, B.-J., Shi, H., & Gasiewski, A. J. (2021). Estimation of Arctic Basin-Scale Sea Ice thickness from satellite passive microwave measurements. *IEEE Transactions on Geoscience and Remote Sensing*, *59*(7), 5841–5850. https://doi.org/10.1109/TGRS.2020.3026949

Lee, S.-M., Sohn, B.-J., & Kim, S.-J. (2017). Differentiating between first-year and multiyear sea ice in the Arctic using microwave-retrieved ice emissivities. *Journal of Geophysical Research: Atmospheres*, *122*(10), 5097–5112. https://doi.org/10.1002/2016JD026275

Lindsay, R., & Schweiger, A. (2013). Unified sea ice thickness climate data record 1947 onward, version 1. https://doi.org/10.7265/N5D50JXV

Madec, G., & Team, N. (2008). *NEMO ocean engine. Note du Pole de modelisation* (p. 396). Institut Pierre-Simon Laplace (IPSL).

Maeda, T., Taniguchi, Y., & Imaoka, K. (2016). GCOM-W1 AMSR2 level 1R product: Dataset of brightness temperature modified using the antenna pattern matching technique. *IEEE Transactions on Geoscience and Remote Sensing*, *54*(2), 770–782. https://doi.org/10.1109/TGRS.2015.2465170

Markus, T., & Cavalieri, D. J. (2009). The AMSR-E NT2 sea ice concentration algorithm: Its basis and implementation. *Journal of The Remote Sensing Society of Japan*, *29*(1), 216–225. https://doi.org/10.11440/rssj.29.216

Meissner, T., Wentz, F. J., & Le Vine, D. M. (2018). The salinity retrieval algorithms for the NASA aquarius version 5 and SMAP version 3 releases. *Remote Sensing*, *10*(7), 1121. https://doi.org/10.3390/rs10071121

Petty, A. A., Kurtz, N. T., Kwok, R., Markus, T., & Neumann, T. A. (2020). Winter Arctic sea ice thickness from ICESat-2 freeboards. *Journal of Geophysical Research: Oceans*, *125*(5), e2019JC015764. https://doi.org/10.1029/2019JC015764

Petty, A. A., Kurtz, N. T., Kwok, R., Markus, T., Neumann, T. A., & Keeney, N. (2022). *ICESat-2 L4 monthly gridded sea ice thickness, version 2*. NASA National Snow and Ice Data Center Distributed Active Archive Center. https://doi.org/10.5067/10.5067/OE8BDP5KU30Q

Petty, A. A., Webster, M., Boisvert, L., & Markus, T. (2018). The NASA Eulerian snow on sea ice model (NESOSIM) v1.0: Initial model development and analysis. *Geoscientific Model Development*, *11*(11), 4577–4602. https://doi.org/10.5194/gmd-11-4577-2018

Pörtner, H.-O., Roberts, D. C., Masson-Delmotte, V., Zhai, P., Tignor, M., Poloczanska, E., & Weyer, N. (2019). The ocean and cryosphere in a changing climate. In *IPCC special report on the ocean and cryosphere in a changing climate*.

Prechelt, L. (2012). Early stopping—But when? In G. Montavon, G. B. Orr, & K.-R. Müller (Eds.), *Neural networks: Tricks of the trade* (2nd ed., pp. 53–67). Springer Berlin Heidelberg. https://doi.org/10.1007/978-3-642-35289-8_5

Prigent, C., & Jimenez, C. (2021). An evaluation of the synergy of satellite passive microwave observations between 1.4 and 36 GHz, for vegetation characterization over the Tropics. *Remote Sensing of Environment*, *257*, 112346. https://doi.org/10.1016/j.rse.2021.112346

Ricker, R., Hendricks, S., Helm, V., Skourup, H., & Davidson, M. (2014). Sensitivity of CryoSat-2 Arctic sea-ice freeboard and thickness on radar-waveform interpretation. *The Cryosphere*, *8*(4), 1607–1622. https://doi.org/10.5194/tc-8-1607-2014

Ricker, R., Hendricks, S., Kaleschke, L., Tian-Kunze, X., King, J., & Haas, C. (2017). A weekly Arctic sea-ice thickness data record from merged CryoSat-2 and SMOS satellite data. *The Cryosphere*, *11*(4), 1607–1623. https://doi.org/10.5194/tc-11-1607-2017

Rodríguez-Fernández, N., de Rosnay, P., Albergel, C., Richaume, P., Aires, F., Prigent, C., & Kerr, Y. (2019). SMOS neural network soil moisture data assimilation in a land surface model and atmospheric impact. *Remote Sensing*, *11*(11), 1334. https://doi.org/10.3390/rs11111334

Rösel, A., Kaleschke, L., & Birnbaum, G. (2012). Melt ponds on Arctic sea ice determined from MODIS satellite data using an artificial neural network. *The Cryosphere*, *6*(2), 431–446. https://doi.org/10.5194/tc-6-431-2012

Rostosky, P., Spreen, G., Farrell, S. L., Frost, T., Heygster, G., & Melsheimer, C. (2018). Snow depth retrieval on Arctic sea ice from passive microwave radiometers—Improvements and extensions to multiyear ice using lower frequencies. *Journal of Geophysical Research: Oceans*, *123*(10), 7120–7138. https://doi.org/10.1029/2018JC014028

Rousset, C., Vancoppenolle, M., Madec, G., Fichefet, T., Flavoni, S., Barthélemy, A., et al. (2015). The Louvain-La-Neuve sea ice model LIM3.6: Global and regional capabilities. *Geoscientific Model Development*, *8*(10), 2991–3005. https://doi.org/10.5194/gmd-8-2991-2015

Rumelhart, D. E., Hinton, G. E., & Williams, R. J. (1985). Learning internal representations by error propagation. Retrieved from https://apps.dtic.mil/sti/citations/ADA164453

Sallila, H., Farrell, S. L., McCurry, J., & Rinne, E. (2019). Assessment of contemporary satellite sea ice thickness products for Arctic sea ice. *The Cryosphere*, *13*(4), 1187–1213. https://doi.org/10.5194/tc-13-1187-2019

Schutz, B. E., Zwally, H. J., Shuman, C. A., Hancock, D., & DiMarzio, J. P. (2005). Overview of the ICESat mission. *Geophysical Research Letters*, *32*(21), L21S01. https://doi.org/10.1029/2005GL024009

Serreze, M. C., & Barry, R. G. (2011). Processes and impacts of Arctic amplification: A research synthesis. *Global and Planetary Change*, *77*(1), 85–96. https://doi.org/10.1016/j.gloplacha.2011.03.004

Soriot, C., Picard, G., Prigent, C., Frappart, F., & Domine, F. (2022). Year-round sea ice and snow characterization from combined passive and active microwave observations and radiative transfer modeling. *Remote Sensing of Environment*, *278*, 113061. https://doi.org/10.1016/j.rse.2022.113061

Stroeve, J. C., Serreze, M. C., Holland, M. M., Kay, J. E., Malanik, J., & Barrett, A. P. (2012). The Arctic's rapidly shrinking sea ice cover: A research synthesis. *Climatic Change*, *110*(3–4), 1005–1027. https://doi.org/10.1007/s10584-011-0101-1

Tian-Kunze, X., Kaleschke, L., Maaß, N., Mäkynen, M., Serra, N., Drusch, M., & Krumpen, T. (2014). SMOS-derived thin sea ice thickness: Algorithm baseline, product specifications and initial verification. *The Cryosphere*, *8*(3), 997–1018. https://doi.org/10.5194/tc-8-997-2014

Tilling, R. L., Ridout, A., & Shepherd, A. (2018). Estimating Arctic sea ice thickness and volume using CryoSat-2 radar altimeter data. *Advances in Space Research*, *62*(6), 1203–1225. https://doi.org/10.1016/j.asr.2017.10.051

Tonboe, R. T., Lavelle, J., Pfeiffer, R.-H., & Howe, E. (2017). Product user manual for OSI SAF global sea ice concentration (Tech. Rep.). EUMETSAT. Retrieved from http://osisaf.met.no/docs/osisaf_cdop3_ss2_pum_ice-conc_v1p5.pdf

Ulaby, F., & Long, D. G. (2014). *Microwave radar and radiometric remote sensing*. The University of Michigan Press.

Verron, J., Sengenes, P., Lambin, J., Noubel, J., Steunou, N., Guillot, A., et al. (2015). The SARAL/AltiKa altimetry satellite mission. *Marine Geodesy*, *38*(1), 2–21. https://doi.org/10.1080/01490419.2014.1000471

Walker, N. P., Partington, K. C., Van Woert, M. L., & Street, T. L. T. (2006). Arctic sea ice type and concentration mapping using passive and active microwave sensors. *IEEE Transactions on Geoscience and Remote Sensing*, *44*(12), 3574–3584. https://doi.org/10.1109/TGRS.2006.881116

Wang, X., Key, J., Kwok, R., & Zhang, J. (2016). Comparison of Arctic sea ice thickness from satellites, aircraft, and PIOMAS data. *Remote Sensing*, *8*(9), 713. https://doi.org/10.3390/rs8090713

Warren, S. G., Rigor, I. G., Untersteiner, N., Radionov, V. F., Bryazgin, N. N., Aleksandrov, Y. I., & Colony, R. (1999). Snow depth on Arctic sea ice. *Journal of Climate*, *12*(6), 16–1829. https://doi.org/10.1175/1520-0442(1999)012<1814:sdoasi>2.0.co;2

Wingham, D., Rapley, C., & Griffiths, H. (1986). New techniques in satellite altimeter tracking systems. *Proceedings of IGARSS*, *86*, 1339–1344.

Yoshizawa, E., Shimada, K., & Cho, K. H. (2018). Algorithm for flat first-year ice draft using AMSR2 data in the Arctic Ocean. *Journal of Atmospheric and Oceanic Technology*, *35*(11), 2147–2157. https://doi.org/10.1175/JTECH-D-18-0034.1